



1 Vertical structure of biomass burning aerosol transported over 2 the southeast Atlantic Ocean

3 Harshvardhan Harshvardhan¹, Richard Ferrare², Sharon Burton², Johnathan Hair², Chris
4 Hostetler², David Harper², Anthony Cook², Marta Fenn³, Amy Jo Scarino³, Eduard Chemyakin³,
5 Detlef Müller⁴

6 ¹Purdue University, West Lafayette, IN, United States

7 ²NASA Langley Research Center, Hampton, VA, United States

8 ³Science Systems and Applications, Inc./NASA Langley Research Center, Hampton, VA, United States

9 ⁴University of Hertfordshire, Hatfield, Hertfordshire, United Kingdom

10 *Correspondence to:* H. Harshvardhan (harshvar@purdue.edu)

11 **Abstract.** Biomass burning in southwestern Africa produces smoke plumes that are transported over the Atlantic
12 Ocean and overlie vast regions of stratocumulus clouds. This aerosol layer contributes to direct and indirect radiative
13 forcing of the atmosphere in this region, particularly during the months of August, September and October. There was
14 a multi-year international campaign to study this aerosol and its interactions with clouds. Here we report on the
15 evolution of aerosol distributions and properties as measured by the airborne high spectral resolution lidar (HSRL)
16 during the ORACLES (Observations of Aerosols above Clouds and their intEractionS) campaign in September 2016.
17 The NASA Langley HSRL-2 instrument was flown on the NASA ER-2 aircraft for several days in September 2016.
18 Data were aggregated at two pairs of 2°×2° grid boxes to examine the evolution of the vertical profile of aerosol
19 properties during transport over the ocean. Results showed that the structure of the profile of aerosol extinction and
20 microphysical properties is maintained over a one to two-day time scale. The fraction of aerosol in the fine mode
21 between 50 and 500 nm remained above 0.95 and the effective radius of this fine mode was 0.16 μm from 3 to 5 km
22 in altitude. This indicates that there is essentially no scavenging or dry deposition at these altitudes. Moreover, there
23 is very little day to day variation in these properties, such that time sampling as happens in such campaigns, may be
24 representative of longer periods such as monthly means. Below 3 km there is considerable mixing with larger aerosol,
25 most likely continental source near land. Furthermore, these measurements indicated that there was a distinct gap
26 between the bottom of the aerosol layer and cloud tops at the selected locations as evidenced by a layer of several
27 hundred meters that contained relatively low aerosol extinction values above the clouds.

28 1 Introduction

29 Aerosols are often considered as the most confounding element in the climate system when simulating future
30 parameters of Earth's climate. Their interaction with clouds makes the problem extremely complicated. The general
31 topic of aerosol-cloud interaction has been of great interest in the scientific community: to quote the report of the
32 Intergovernmental Panel on Climate Change (IPCC AR5) "Clouds and aerosols continue to contribute the largest
33 uncertainty to estimates and interpretations of the Earth's changing energy budget" (Boucher et al., 2013).



34 In the context of these interactions, the interplay of biomass burning (BB) aerosol and the stratocumulus clouds in
35 the South East (SE) Atlantic is unique and crucial to the estimates of the energy budget of the region. This BB aerosol
36 arises from the seasonal burning (July-October) of agricultural residue in the southwestern African Savannah and
37 traverses large distances westward over the SE Atlantic Ocean. Unlike the aerosol from industrial activity and biofuels
38 that intermingle with clouds in many regions (Ramanathan et al., 2001; Mechoso et al., 2013), these optically thick
39 BB aerosol layers overly vast stretches of marine stratus cloud in the SE Atlantic (Chand et al., 2009; Wilcox, 2010;
40 Adebisi et al., 2015) where they have a direct radiative effect. The BB aerosol can also act as nuclei for cloud droplets
41 and so cause a potentially significant cloud albedo effect. There is also some evidence that aerosol can alter the
42 thermodynamics of cloud formation through semi-direct effects (Sakaeda et al., 2011). Studies using high resolution
43 limited area models have shown a variety of effects, including stratus to cumulus transition resulting from these
44 interactions (Yamaguchi et al., 2015; Gordon et al., 2018; Lu et al., 2018). The semi-direct effect has also been shown
45 to be important in a limited time run of a global model (Das et al., 2020).

46 During the course of its transport over the Atlantic basin, the dense BB aerosol layer affects the underlying clouds
47 and Earth's radiative balance in multiple ways. It exerts a direct radiative forcing (DRF) on the atmosphere by mostly
48 absorbing the incoming solar radiation along with the radiation reflected by the underlying cloud surface (Chand et
49 al., 2009; Meyer et al., 2013; Zhang et al., 2016). Simultaneously, depending on the relative vertical location of the
50 aerosol with respect to the cloud deck, the cloud cover (fraction) or liquid water path may increase or decrease in
51 response to heating of surrounding air masses due to aerosol absorption and subsequent changes in atmospheric
52 stability, the semi-direct forcing (Sakaeda et al., 2011; Wilcox, 2012; Das et al., 2020). Moreover, as the marine
53 boundary layer (MBL) deepens farther offshore and north of 5° S, subsiding aerosol particles become entrained into
54 the MBL and interact with the clouds as cloud condensation nuclei to affect their microphysics (indirect forcing)
55 (Costantino and Breon, 2013; Painemal et al., 2014).

56 In the context of simulating the above alluded aerosol radiative effects, it is vital that aerosol-cloud overlap
57 characteristics are accurately represented within the models. The quantification of these aerosol-cloud overlap
58 characteristics in the models is necessary for a variety of reasons. For example, previous studies have found that the
59 sign and magnitude of DRF of absorbing aerosol above clouds (AAC) critically depends upon the reflectance and
60 coverage of the underlying cloud surfaces along with the optical properties, composition and size distribution of the
61 overlying aerosols (Keil and Haywood, 2003; Chand et al., 2009). Additionally, the magnitude and sign of the aerosol
62 semi-direct effects are quite sensitive to the vertical distribution of aerosols, especially with respect to the vertical
63 location of clouds (Penner et al., 2003; McFarquhar and Wang, 2006; Koch and Del Genio, 2010).

64 Here we address the evolution of the vertical properties of BB aerosol as it travels in the marine environment after
65 leaving the African land mass. Section 2 identifies the field campaign and specifies the geographic region selected for
66 the analysis and rationale for that choice. Section 3 describes the attributes of the instrument and key parameters
67 related to the aerosol that can be extracted from the measurements. Section 4 presents the results followed by a
68 summary and conclusion in section 5.

69
70



71

72 2 Field Campaigns

73 The concerns mentioned above were the driving force behind plans for several international multi-year field
74 campaigns; ORACLES (Observations of Aerosols above Clouds and their intERactionS, Redemann et al., 2021),
75 CLARIFY-2017 (CLOUD-Aerosol-Radiation Interactions and Forcing for Year 2017, Wu et al., 2020), and LASIC
76 (Layered Atlantic Smoke Interactions with Clouds, Zuidema et al., 2016, 2018). A key component of the September
77 2016 NASA ORACLES Intensive Observation Period (IOP) was the vertical profiling of aerosol properties measured
78 by an airborne lidar, the NASA Langley High Spectral Resolution Lidar-2, HSRL-2 (Burton et al., 2018), on-board
79 the NASA ER-2, which was based in Walvis Bay, Namibia, for operations during 2016. In the following two years,
80 the instrument was on-board the P-3 flying out of São Tomé. The siting and flight tracks chosen ensured adequate
81 coverage of the seasonal BB aerosol. The overall meteorological situation is shown in Fig. 1 from MERRA2 reanalysis
82 (Buchard et al., 2017; Randles et al., 2017) along with locations of relevant sites. ER-2 flight tracks during the
83 September 2016 IOP are shown in Fig. 2. Note that flights were primarily confined to roughly 1000 km of the African
84 coast with only the 22 September flight venturing further. Flights such as executed during the IOP are unable to follow
85 air parcels in a Lagrangian fashion to examine the evolution of smoke plumes. Here we provide an alternate frame by
86 which to study evolving aerosol properties in an average sense. In order to establish average characteristics of the BB
87 smoke plume as it travels over the ocean, we have chosen five grid boxes of two-degree latitude and longitude on a
88 side at various distances from the source and aggregated observations. The choice of grid boxes was based on the
89 availability of data from the flights and the general direction of transport of the smoke based on backward trajectory
90 analyses. Figure 3 shows 48-hour backward trajectory frequency analyses at 3.5 km, roughly the central altitude of
91 the plume, using NOAA HYSPLIT trajectory calculations (https://www.ready.noaa.gov/HYSPLIT_traj.php) which
92 were carried out using archived GDAS 0.5-degree meteorology (Stein et al., 2015). The frequency distribution is a
93 48-hour history of the paths taken by air parcels arriving at the center of grid boxes marked A and C at 3500 m altitude.
94 The time period of the frequency analyses covers the entire period during which HSRL-2 measurements were made,
95 12-24 September 2016. The selected grid box pairs indicate that Box A receives aerosol that has earlier crossed Box
96 B and Box C is downwind of Box D; boxes B and D receive aerosol directly from BB sources on land. The grid box
97 pairs A/B and C/D can therefore provide information on the evolution of the microphysics and vertical distribution of
98 BB aerosol plumes after leaving the continent. This strategy is similar to that used in comparisons of models with
99 observations for this campaign by Shinozuka et al. (2020), who also showed that observations made on the sampled
100 days were representative of monthly means. In addition to the four boxes strongly influenced by smoke, a southern
101 box, E, has been chosen to provide a control contrast to the other areas in that it is influenced primarily by maritime
102 air as seen from Fig. 1. The location of the five grid boxes is also shown superimposed on flight tracks in Fig. 2.

103 The days during the campaign that were included in the averaging procedure are shown in Table 1. Also included
104 is the typical time of the day when the measurements were made, a function of the flight pattern of the ER-2. The
105 number of lidar return profiles averaged for each grid box and statistics related to the backward trajectories are also



106 listed. These grid boxes contained aircraft tracks on multiple days during which trajectory analysis showed near-
107 uniform wind direction between 2.5 and 4.5 km altitude throughout the IOP. With the exception of the grid box
108 centered at 22° S, 9° E, all indicate flow from the source region of BB aerosol. Table 1 also lists the mean and standard
109 deviation of time duration in hours spent over water of air parcels arriving at 3500 m altitude at the grid box center
110 during the averaging period. There is no entry for Box E since arriving air had a maritime source and did not originate
111 from land. It must be stressed that the duration is not calculated from the source region on land, which is distributed
112 over a large area of central Africa (e.g., Fig. 9 of Redemann et al., 2021) and cannot be uniquely identified with
113 specific observations made over the ocean. The plume has already been airborne over land for several hours (see Fig.
114 3) and aerosol would have undergone transformations that occur at short time scales (Cappa et al., 2020). The duration
115 was calculated by running HYSPLIT backward trajectories of air parcels arriving every six hours starting at 0600
116 UTC on the days of the first flight and ending at 1800 UTC on the days of the last flight of the averaging period and
117 is shown in some detail in Fig. 4, which essentially reflects the profile of the prevailing wind speeds. The inference is
118 that BB smoke at 3500 m altitude arrives at A on average about 30 h after passing B and arrives at C 35 h after passing
119 D. The change in selected aerosol properties as measured by the HSRL-2 during this travel in the marine environment
120 provides information on the evolution of the plume during this time period.

121 3 HSRL-2

122 The NASA LaRC HSRL-2 uses the HSRL technique to independently retrieve aerosol and tenuous cloud extinction
123 and backscatter (Shiple et al., 1983; Grund and Eloranta, 1991; She et al., 1992) without a priori assumptions on
124 aerosol type or extinction-to-backscatter ratio. By using the HSRL technique, HSRL-2, like its predecessor HSRL-1
125 (Hair et al., 2008), provides accurate backscatter profiles even in situations where the lidar beam is attenuated by
126 overlying cloud or aerosol as long as it is not completely attenuated. The LaRC HSRL-2 employs the HSRL technique
127 at 355 and 532 nm and the standard backscatter technique at 1064 nm. It also measures aerosol and cloud
128 depolarization at all three wavelengths. The HSRL-2 provides vertically resolved measurements of the following
129 extensive and intensive aerosol parameters below the aircraft (approximate archival horizontal, Δx , and vertical
130 resolutions, Δz , are listed assuming ER-2 cruise speed).

131 • *Extensive parameters*¹ – backscatter coefficient, β , at 355, 532 and 1064 nm ($\Delta x \sim 2$ km, $\Delta z \sim 15$ m);
132 extinction coefficient, α , at 355, and 532 nm ($\Delta x \sim 12$ km, $\Delta z \sim 300$ m); optical depth at 355 and 532 nm (integrating
133 the profile of extinction). The aerosol optical depth (AOD), is a critical quantity in discussions of the influence of
134 aerosol on climate (Boucher et al., 2013).

¹ By the term *extensive*, we refer to optical parameters, such as extinction, that are influenced by the amount (concentration) and type (size, composition, shape) of aerosol/cloud particles. *Intensive* properties, on the other hand, are those that depend only on the nature of the particles and not on their quantity or concentration, but rather depend only on aerosol type (Anderson et al., 2003).



135 • *Intensive parameters* – extinction-to-backscatter ratio of aerosol, the Lidar Ratio, $S_a = \alpha_a / \beta_a$, at 355 and
136 532 nm ($\Delta x \sim 12$ km, $\Delta z \sim 300$ m); depolarization, $\delta_a = \beta_a^\perp / \beta_a^\parallel$, at 355, 532, and 1064 nm ($\Delta x \sim 2$ km, $\Delta z \sim 15$ m);
137 and aerosol backscatter wavelength dependence (i.e., Ångström exponent for aerosol backscatter – directly related to
138 the backscatter color ratio) for two wavelength pairs (355-532 and 532-1064 nm, $\Delta x \sim 2$ km, $\Delta z \sim 15$ m).

139 The overall systematic error associated with the backscatter calibration is estimated to be less than 5 % for the 355
140 and 532 nm channels and 20 % for 1064 nm (Burton et al., 2015). Under typical conditions, the total systematic error
141 for extinction is estimated to be less than 0.01 km^{-1} at 532 nm. The random errors for all aerosol products are typically
142 less than 10 % for the backscatter and depolarization ratios (Hair et al., 2008). Rogers et al. (2009) validated the HSRL
143 extinction coefficient profiles and found that the HSRL extinction profiles are within the typical state-of-the-art
144 systematic error at visible wavelengths (Schmid et al., 2006). Since HSRL-2 includes the capability to measure
145 backscatter at three wavelengths and extinction at two wavelengths, “ $3\beta+2\alpha$ ” microphysical retrieval algorithms
146 (Müller et al., 1999a, 1999b; Veselovskii et al., 2002) are used to retrieve height-resolved parameters such as aerosol
147 effective radius and number, surface and volume concentrations (Müller et al., 2014, Sawamura et al., 2016).

148 4 Results

149 In this study of the vertically resolved evolving properties of BB aerosol, we present key lidar measurements and
150 microphysical results obtained by performing the “ $3\beta+2\alpha$ ” retrieval mentioned in Section 3.

151 4.1 Lidar

152 Vertical profiles averaged over the times of overflight in $2^\circ \times 2^\circ$ latitude/longitude boxes shown in Figure 3 on the
153 days given in Table 1 are for the following properties.

- 154 1. Aerosol Extinction at 532 nm, α_a , the primary measure of aerosol abundance.
- 155 2. Backscatter Ångström exponent between 1064 and 532 nm, an indication of particle size.
- 156 3. Aerosol Depolarization at 532 nm, a measure of particle asphericity.
- 157 4. Aerosol extinction to backscatter ratio, the Lidar Ratio, at 532 nm, a marker for aerosol composition.

158 Inspection of the wind field at 650 hPa in Fig. 1 and backward trajectory frequency plots in Fig. 3 suggest that the
159 grid boxes chosen fit naturally into two pairs of tracks of the widespread BB aerosol field. The northern pair, identified
160 in Table 1 and Fig. 3 as A and B, centered around 10° S, are in a faster zonal track, whereas the grid boxes C and D
161 are in a track centered between 13 - 15° S that is slightly slower and has a component from the north over a stretch of
162 water. The two pairs can then provide information on the evolution of aerosol properties over a time scale of one to
163 two days. Figures 5-8 show the aerosol extinction, backscatter Ångström exponent, depolarization and Lidar Ratio for
164 the two pairs of grid boxes and Box E, which is not significantly influenced by the BB aerosol. The results presented
165 are one-minute averages of independent 10 s vertical profiles for backscatter Ångström exponent and depolarization



166 and one-minute averages for extinction and lidar ratio profiles. From Table 1, the mean time elapsed between B and
167 A is 29.4 h and that between D and C is 34.9 h. It should be pointed out that parameter values shown below the level
168 of mean cloud top are averages of lidar returns through breaks in the stratus deck and are not relevant for this study.
169 If we use the low cut-off of an extinction coefficient of 15 Mm^{-1} to indicate an aerosol-free layer (Shinozuka et al.,
170 2020), then Fig. 6 indicates that the bulk of the smoke layers encountered at these distances from land were separated
171 from the cloud top, a feature more prevalent during the 2016 IOP (Redemann et al., 2021).

172 The northern plume is a column of aerosol of essentially constant extinction from just above 2.5 km to 5 km while
173 the southern plume has a profile of extinction that increases nearly linearly with height from a minimum near the cloud
174 top to a maximum at 5 km. The Ångström exponent and depolarization indicate the presence of fine spherical particles
175 at the top of the plume and increasing sizes towards the bottom. The Lidar Ratio above 3 km for the two pairs is
176 between 70 and 80 sr, suggesting strong absorption (Müller et al., 2019) but is considerably less and highly variable
177 in Box E and in the lower layers of the aerosol plume in Box D, where the plume most likely has components of
178 continental aerosol typical of the nearby Namibian coast (Klopper et al., 2020). The most striking feature of the results
179 are the near constant values of these parameters in the upper two kilometers of the plume over the course of several
180 days as evident from the range of values in the 25-75 percentile shaded grey in Figs. 6 and 7. This suggests strongly
181 that the original particles near the source of combustion have been coated before they cross the land-ocean boundary
182 and maintain their size over the first few days of transport over the ocean. The lower portion of the plume containing
183 larger BB aerosol particles is subject to mixing with other particles and is highly variable in nature. This result is of
184 some importance for climate studies in which the radiative properties of BB aerosol are input to the calculation of
185 radiative forcing. Complex chain aggregates as found near the source of fires (Pósfai et al., 2003, China et al., 2013)
186 are typically not represented in climate models. However, if the aerosol is already coated and maintains its size over
187 the time period of radiative interactions being studied, then core-shell models of varying degrees of complexity could
188 perhaps suffice (Zhang et al., 2020).

189 4.2 Microphysics

190 The lidar measurements are inverted to obtain information regarding particle size. The inversion is performed on one-
191 minute averages of six independent 10 s backscatter profiles and one-minute average extinction profiles. Details of
192 the inversion process are in Müller et al. (2019) and references therein. The particle size distribution is represented
193 using a series of eight triangular basis functions that can represent both monomodal and bimodal size distributions
194 (*ibid*). Points to note are that the procedure makes the following assumptions: the particles are spherical and
195 homogeneous having wavelength-independent complex index of refraction. The low ($< 5\%$) values of depolarization
196 through most of the plume, shown in Fig. 7, suggests that the spherical assumption is justified. There is most likely
197 structure and inhomogeneity in the core of the particles but current particle optical models are unable to incorporate
198 these complexities. Results from this inversion procedure have been compared to coincident airborne in situ particle
199 measurements. Müller et al. (2014) present results from a campaign off the northeast coast of the US showing that the
200 inversion results agree with in situ measurements of effective radius and also number, surface area and volume



201 concentration within error bars. Sawamura et al. (2017) report on campaigns in the wintertime San Joaquin Valley of
202 California and summertime near Houston, TX. They found high correlation and low bias in surface and volume
203 concentration in situ measurements relative to HSRL with the best agreement for submicron fine-mode aerosol, which
204 is most relevant to the current study. Müller et al. (2019) report retrievals and their uncertainty for one day in the
205 ORACLES campaign, 22 September 2016. Considering only optical data with strong signal-to-noise ratio, they
206 estimate retrieval errors are 25 % for number concentration. The relative uncertainty in effective radius for parts of
207 the flight track where particle size was nearly constant was below 20 %.

208 In order to help separate particles that have BB source from coarser particles of continental or marine origin, we
209 specify a Submicron Fraction (SMF) as the contribution to the extinction at 532 nm of particles in the radius range 50
210 nm–500 nm (Anderson et al., 2005). Figure 9 shows the profiles of SMF for the five grid boxes and not surprisingly,
211 the bulk of the smoke plume, especially between 3 and 5 km contains aerosol almost entirely in the sub-micron range.
212 Below 3 km, at locations both near and further way from the coast, there is a marked increase in the fraction of larger
213 particles. The increase in depolarization (Fig. 7) at these lower levels and a decrease in the Lidar Ratio (Fig. 8) suggest
214 mixing with continental and marine particles. However, the sharp decrease in extinction below 3 km (Fig. 5) indicates
215 that their contribution to direct radiative effects would be minimal. Finally, Fig. 10 shows the vertical profile of the
216 effective radius of the SMF aerosol population. The effective radius is $0.16 \pm 0.1 \mu\text{m}$ with little variation throughout the
217 vertical extent of the plume. Of greater significance is that it remains very similar between the pairs of grid boxes
218 along the transport trajectory of the smoke. The retrieved effective radius is similar to the results presented by Müller
219 et al. (2014) for a mixture of urban aerosol and smoke. Their comparison with in situ measurements showed a slight
220 overestimate but within a standard deviation. The retrieved and in situ results also show that the particle size is uniform
221 with altitude even when the number concentration drops by a factor of three. Another set of prior comparisons of
222 HSRL-2 and in situ measurements is provided in Sawamura et al. (2017). Here again, the effective radius of the
223 submicron fraction of particles, $0.15 \mu\text{m}$, is uniform with altitude, and comparable though biased slightly low.

224 5 Conclusions

225 The results of the aggregated HSRL-2 profiles during the 2016 ORACLES IOP presented here show two main
226 findings. These are however limited to a brief period in the transport of BB smoke from continental Africa over marine
227 clouds in the Atlantic Ocean. This is a limitation of the 2016 campaign because the flight tracks remained within 1000
228 km of the coast. For the period of one to two days after crossing the land-ocean boundary, the fraction of all particles
229 that are in the submicron range in the main smoke plume between 3 and 5 km is around 95 %. The effective radius of
230 the particles in this range is $0.15\text{--}0.16 \mu\text{m}$ and constant with altitude. The particle size is comparable to measured
231 particle sizes in previous campaigns that sampled aerosol that was a mixture of urban haze and smoke (Müller et al.,
232 2014; Sawamura et al., 2017). Moreover, the shape of the median vertical profile of extinction does not change during
233 the first two days of transport over water suggesting the absence of dry deposition and wet scavenging. The low ($<$
234 0.05) depolarization ratio of the submicron particles signify that they are well coated and the assumption of sphericity
235 in the inversion procedure and models that estimate the radiative effects of aerosol is justified. The BB aerosol mix



236 with continental and marine aerosol at the base of the plume but during the September 2016 IOP this layer of mixed
237 aerosol tended to be very tenuous and there was a distinct gap between the plume and the cloud tops.

238 The HSRL-2 instrument was also deployed in the 2017 and 2018 ORACLES campaigns but was mounted on a P-3
239 which often flew at low altitude to acquire in situ measurements of aerosols and clouds. Consequently, the HSRL2
240 was not able to make continuous measurements of the BB aerosol plumes in a manner similar as when deployed on
241 the ER-2. However, there are segments of the track that can provide information similar to those obtained in the 2016
242 campaign but for a different time period. Moreover, some flight tracks extended much further from land (Doherty et
243 al., 2021). Analysis of the later campaigns will provide information on the physical evolution of aerosol that has aged
244 for a longer period than is covered in this study.

245 **Data Management**

246 HSRL-2 optical data and retrieved inversion data are available at the NASA archive site
247 <https://espoarchive.nasa.gov/archive/browse/oracles/id8/ER2> and are permanently archived at
248 doi:10.5067/SUBORBITAL/ORACLES/ER2/2016_V1.

249 **Acknowledgements**

250 The lead author would like to thank NASA Langley Research Center for hosting him during a sabbatical when this
251 study was initiated. HSRL-2 participation in ORACLES was supported by NASA through the Earth Venture
252 Suborbital-2 (EVS-2) program (grant no. 13-EVS2-13-0028). Funding for this work was also provided by NASA
253 through the Radiation Sciences Program. We wish to thank the NASA ER-2 pilots and ground crew for their extensive
254 support during ORACLES.

255



256 References

- 257 Anderson, T. L., Charlson, R. J., Winker, D. M., Ogren, J. A., and Holmén, K.: Mesoscale variations of tropospheric
258 aerosols, *J. Atmos. Sci.*, 60(1), 119-136, 2003.
- 259 Anderson, T. L., Wu, Y., Chu, D. A., Schmid, B., Redemann, J., and Dubovik, O.: Testing the MODIS satellite
260 retrieval of aerosol fine-mode fraction, *J. Geophys. Res.*, 110, D18204, doi:10.1029/2005JD005978, 2005.
- 261 Adebiyi, A. A., Zuidema, P., Chang, I., Burton, S. P., and Cairns, B.: Mid-level clouds are frequent above the Southeast
262 Atlantic stratocumulus clouds, *Atmos. Chem. Phys.*, 20, 11025-11043, doi:10.5194/acp-20-11025-2020, 2020.
- 263 Boucher, O., Randall, D., Artaxo, P., Bretherton, C., Feingold, G., Forster, P., Kerminen, V.-M., Kondo, Y., Liao, H.,
264 Lohmann, U., Rasch, P., Satheesh, S. K., Sherwood, S., Stevens, B., and Zhang X.Y.: Clouds and Aerosols. In:
265 *Climate Change 2013: The Physical Science Basis. Contribution of Working Group I to the Fifth Assessment Report*
266 *of the Intergovernmental Panel on Climate Change* [Stocker, T. F., Qin, D., Plattner, G.-K., Tignor, M., Allen, S.
267 K., Boschung, J., Nauels, A., Xia, Y., Bex V., and Midgley, P. M. (eds.)]. Cambridge University Press, 2013.
- 268 Buchard, V., Randles, C. A., da Silva, A. M., Darmenov, A., Colarco, P. R., Govindaraju, R., Ferrare, R. A., Hair, J.,
269 Beyersdorf, A. J., Ziemba L. D., and Yu, H.: The MERRA-2 aerosol reanalysis, 1980 onwards Part II: Evaluation
270 and case studies, *J. Climate*, 30, 6851-6871, doi:10.1175/JCLI-D-16-0613.1, 2017.
- 271 Burton, S. P., Hostetler, C. A., Cook, A. L., Hair, J. W., Seaman, S., Scola, S., Harper, D. B., Smith, J. A., Fenn, M
272 A., Ferrare, R. A., Saide, P. E., Chemyakin, E. V., and Müller, D.: Calibration of a high spectral resolution lidar
273 using a Michelson interferometer with data examples from ORACLES, *Appl. Optics*, 57, 6061-6075, 2018.
- 274 Burton, S. P., Hair, J. W., Kahnert, M., Ferrare, R. A., Hostetler, C. A., Cook, A. L., Harper, D. B., Berkoff, T. A.,
275 Seaman, S. T., Collins, J. E., Fenn, M. A., and Rogers, R. R.: Observations of the spectral dependence of linear
276 particle depolarization ratio of aerosols using NASA Langley airborne High Spectral Resolution Lidar, *Atmos.*
277 *Chem. Phys.*, 15, 13453-13473, doi.org/10.5194/acp-15-13453-2015, 2015.
- 278 Cappa, C. D., Lim, C. Y., Hagan, D. H., Coggon, M., Koss, A., Sekimoto, K., de Gouw, J., Onasch, T. B., Warneke,
279 C., and Kroll, J. H.: Biomass-burning-derived particles from a wide variety of fuels – Part 2: Effects of
280 photochemical aging on particle optical and chemical properties, *Atmos. Chem. Phys.*, 20, 8511-8532,
281 doi:10.5194/acp-20-8511-2020, 2020.
- 282 Chand, D., Wood, R., Anderson, T. L., Satheesh, S. K., and Charlson, R. J.: Satellite-derived direct radiative effect of
283 aerosols dependent on cloud cover, *Nat. Geosci.*, 2, 181-184, doi:10.1038/Ngeo437, 2009.
- 284 China, S., Mazzoleni, C., Gorkowski, K., Aiken, A. C., and Dubey, M. K.: Morphology and mixing state of individual
285 freshly emitted wildfire carbonaceous particles, *Nat. Commun.*, 4:2122 doi: 10.1038/ncomms3122, 2013.
- 286 Costantino, L., and Bréon F. M.: Aerosol indirect effect on warm clouds over South-East Atlantic from co-located
287 MODIS and CALIPSO observations, *Atmos. Chem. Phys.*, 13, 69-88, doi:10.5194/acp-13-69-2013, 2013.
- 288 Das, S., Harshvardhan, H., and Colarco, P. R.: The influence of elevated smoke layers on stratocumulus clouds over
289 the SE Atlantic in the NASA Goddard Earth Observing System (GEOS) Model, *J. Geophys. Res. Atmos.*, 125,
290 e2019JD031209. doi:10.1029/2019JD031209, 2020.
- 291 Doherty, S. J., Saide, P. E., Zuidema, P., Shinozuka, Y., Ferrada, G. A., Gordon, H., Mallet, M., Meyer, K.,
292 Painemal, D., Howell, S. G., Freitag, S., Dobracki, A., Podolske, J. R., Burton, S. P., Ferrare, R. A., Howes, C.,
293 Nabat, P., Carmichael, G. R., da Silva, A., Pistone, K., Chang, I., Gao, L., Wood, R., and Redemann, J.: Modeled
294 and observed properties related to the direct aerosol radiative effect of biomass burning aerosol over the Southeast
295 Atlantic, *Atmos. Chem. Phys. Discuss.* [preprint], <https://doi.org/10.5194/acp-2021-333>, in review, 2021.
- 296 Gordon, H., Field, P. R., Abe, S. J., Dalvi, M., Grosvenor, D. P., Hill, A. A., Johnson, B. T., Miltenberger, A. K.,
297 Yoshioka, M., and Carslaw, K. S.: Large simulated radiative effects of smoke in the south-east Atlantic, *Atmos.*
298 *Chem. Phys.*, 18, 15261-15289, doi:10.5194/acp-18-15261-2018, 2018.
- 299 Grund, C. J., and Eloranta, E. W.: University of Wisconsin high spectral resolution lidar, *Opt. Eng.*, 30, 6-12, 1991.
- 300 Hair, J. W., Hostetler, C. A., Cook, A. L., Harper, D. B., Ferrare, R. A., Mack, T. L., Welch, W., Izquierdo, L. R.,
301 Hovis, F. E.: Airborne High Spectral Resolution Lidar for profiling aerosol optical properties, *Appl. Optics*, 47, doi:
302 10.1364/AO.47.006734, 2008.
- 303 Keil, A., and Haywood, J. M.: Solar radiative forcing by biomass burning aerosol particles during SAFARI 2000: A
304 case study based on measured aerosol and cloud properties, *J. Geophys. Res. Atmos.*, 108, 8467,
305 doi:10.1029/2002JD002315, 2003.
- 306 Klopper, D., Formenti, P., Namwoonde, A., Cazaunau, M., Chevallier, S., Feron, A., Gaimoz, C., Hease, P., Lahmidi,
307 F., Mirande-Bret, C., Triquet, S., Zeng, Z., and Piketh, S. J.: Chemical composition and source apportionment of
308 atmospheric aerosols on the Namibian coast, *Atmos. Chem. Phys.*, 20, 15,811-15,833, doi:10.5194/acp-20-15811-
309 2020, 2020.



- 310 Koch, D., and Del Genio A. D.: Black carbon semi-direct effects on cloud cover: review and synthesis, *Atmos. Chem.*
311 *Phys.*, 10, 7685-7696, doi:10.5194/acp-10-7685-2010, 2010.
- 312 Lu, Z., Liu, X., Zhang, Z., Zhao, C., Meyer, K., Rajapakse, C., Wu, C., Yang, Z., and Penner, J.: Biomass smoke
313 from southern Africa can significantly enhance the brightness of stratocumulus over the southeastern Atlantic
314 Ocean, *Proc. Natl. Acad. Sc.*, 115, 2924-2929, doi:10.1073/pnas.1713703115, 2018.
- 315 McFarquhar, G. M., and Wang, H.: Effects of aerosols on trade wind cumuli over the Indian Ocean: Model
316 simulations, *Q. J. R. Meteorol. Soc.*, 132, 821-843, doi: 10.1256/qj.04.179, 2006.
- 317 Mechoso, C. R., Wood, R., Weller, R., Bretherton, C. S., Clarke, A. D., Coe, H., Fairall, C., Farrar, J. T., Feingold,
318 G., Garreaud, R., Grados, C., McWilliams, J., de Szoeke, S. P., Yuter, S. E., and Zuidema, Z.: Ocean–cloud–
319 atmosphere–land interactions in the Southeastern Pacific: The VOCALS program, *B. Am. Meteorol. Soc.*, 95, 357-
320 375, doi:10.1175/BAMS-D-11-00246.1, 2013.
- 321 Meyer, K., Platnick, S., Oreopoulos, L., and Lee, D.: Estimating the direct radiative effect of absorbing aerosols
322 overlying marine boundary layer clouds in the southeast Atlantic using MODIS and CALIOP, *J. Geophys. Res.*
323 *Atmos.*, 118, 4801–4815, doi:10.1002/jgrd.50449, 2013.
- 324 Müller, D., Wandinger, U., and Ansmann, A.: Microphysical particle parameters from extinction and backscatter lidar
325 data by inversion with regularization: theory, *Appl. Optics*, 38, 2346-2357, 1999a.
- 326 Müller, D., Wandinger, U., and Ansmann, A.: Microphysical particle parameters from extinction and backscatter lidar
327 data by inversion with regularization: simulation, *Appl. Optics*, 38, 2358-2368, 1999b.
- 328 Müller, D., Hostetler, C. A., Ferrare, R. A., Burton, S. P., Chemyakin, E., Kolgotin, A., Hair, J. W., Cook, A. L.,
329 Harper, D. B., Rogers, R. R., Hare, R. W., Cleckner, C. S., Obland, M. D., Tomlinson, J. Berg, L. K., and Schmid,
330 B.: Airborne multiwavelength high spectral resolution lidar (HSRL-2) observations during TCAP 2012: vertical
331 profiles of optical and microphysical properties of a smoke/urban haze plume over the northeastern coast of the US,
332 *Atmos. Meas. Tech.*, 7, 3487-3496, doi:10.5194/amt-7-3487-2014, 2014.
- 333 Müller, D., Chemyakin, E., Kolgotin, A., Ferrare, R. A., Hostetler, C. A., and Romanov, A.: Automated, unsupervised,
334 inversion of multiwavelength lidar data with TiARA: assessment of retrieval performance of microphysical
335 parameters using simulated data, *Appl. Optics*, 58, 4981-5007, doi:10.1364/AO.58.004981, 2019.
- 336 Painemal, D., Kato, S., and Minnis, P.: Boundary layer regulation in the southeast Atlantic cloud microphysics during
337 the biomass burning season as seen by the A-train satellite constellation, *J. Geophys. Res. Atmospheres*, 119,
338 11,288-211,302, doi:10.1002/2014JD022182, 2014.
- 339 Penner, J. E., Zhang, S. Y., and Chuang, C. C.: Soot and smoke aerosol may not warm climate, *J. Geophys. Res.*
340 *Atmospheres*, 108, 4657, doi:10.1029/2003JD003409, 2003.
- 341 Pósfai, M., Simonić, R., Li, J., Hobbs, P. V., and Buseck, P. R.: Individual aerosol particles from biomass burning in
342 southern Africa: 1. Compositions and size distributions of carbonaceous particles, *J. Geophys. Res.*, 108, 8483,
343 doi:10.1029/2002JD002291, 2003.
- 344 Ramanathan, V., Crutzen, P. J., Kiehl, J. T., and Rosenfeld, D.: Aerosols, climate, and the hydrological cycle, *Science*,
345 294(5549), 2119-2124, doi:10.1126/science.1064034, 2001.
- 346 Randles, C.A., daSilva, A. M., Buchard, V., Colarco, P. R., Darmenov, A., Govindaraju, P., Smirnov, A., Holben, B.,
347 Ferrare, R. A., Hair, J., Shinozuka, Y., and Flynn, C. J.: The MERRA-2 aerosol reanalysis, 1980 onward. Part I:
348 System description and data assimilation evaluation, *J. Climate*, 30, 6823–6850, doi: 10.1175/JCLI-D-16-0609.1,
349 2017.
- 350 Redemann, J., Wood, R., Zuidema, P., Doherty, S. J., Luna, B., LeBlanc, S. E., Diamond, M. S., Shinozuka, Y., Chang,
351 I. Y., Ueyama, R., Pfister, L., Ryoo, J.-M., Dobracki, A. N., da Silva, A. M., Longo, K. M., Kacenenbogen, M.
352 S., Flynn, C. J., Pistone, K., Knox, N. M., Piketh, S. J., Haywood, J. M., Formenti, P., Mallet, M., Stier, P.,
353 Ackerman, A. S., Bauer, S. E., Fridlind, A. M., Carmichael, G. R., Saide, P. E., Ferrada, G. A., Howell, S. G.,
354 Freitag, S., Cairns, B., Holben, B. N., Knobelspiesse, K. D., Tanelli, S., L'Ecuyer, T. S., Dzambo, A. M., Sy, O. O.,
355 McFarquhar, G. M., Poellot, M. R., Gupta, S., O'Brien, J. R., Nenes, A., Kacarab, M., Wong, J. P. S., Small-
356 Griswold, J. D., Thornhill, K. L., Noone, D., Podolske, J. R., Schmidt, K. S., Pilewskie, P., Chen, H., Cochrane, S.
357 P., Sedlacek, A. J., Lang, T. J., Stith, E., Segal-Rozenhaimer, M., Ferrare, R. A., Burton, S. P., Hostetler, C. A.,
358 Diner, D. J., Seidel, F. C., Platnick, S. E., Myers, J. S., Meyer, K. G., Spangenberg, D. A., Maring, H., and Guo, L.:
359 An overview of the ORACLES (ObseRvations of Aerosols above Clouds and their intERactionS) project: aerosol-
360 cloud-radiation interactions in the southeast Atlantic basin, *Atmos. Chem. Phys.*, 21, 1507-1563, doi:10.5194/acp-
361 21-1507-2021, 2021.
- 362 Rogers, R. R., Hair, J. W., Hostetler, C. A., Ferrare, R. A., Obland, M. D., Cook, A. L., Harper, D. B., Burton, S. P.,
363 Shinozuka, Y., McNaughton, C. S., Clarke, A. D., Redemann, J., Russell, P. B., Livingston, J. M., and Kleinman,
364 L. I.: NASA LaRC airborne high spectral resolution lidar aerosol measurements during MILAGRO: observations
365 and validation, *Atmos. Chem. Phys.*, 9, 4811-4826, 2009.



- 366 Sakaeda, N., Wood, R., and Rasch, P. J.: Direct and semidirect aerosol effects of southern African biomass burning
367 aerosol, *J. Geophys. Res. Atmospheres*, 116, D12205, doi:10.1029/2010JD015540, 2011.
- 368 Sawamura, P., Moore, R. H., Burton, S. P., Chemyakin, E., Müller, D., Kolgotin, A., Ferrare, R. A., Hostetler, C. A.,
369 Ziemba, L. D., Beyersdorf, A. J., and Anderson, B. E.: HSRL-2 aerosol optical measurements and microphysical
370 retrievals vs. airborne in situ measurements during DISCOVER-AQ 2013: an intercomparison study, *Atmos. Chem.*
371 *Phys.*, 17, 7229-7243, doi.org/10.5194/acp-17-7229-2017, 2017.
- 372 Schmid, B., Ferrare, R. A., Flynn, C., Elleman, R., Covert, D., Strawa, A., Welton, E., Turner, D., Jonsson, H.,
373 Redemann, J., Eilers, J., Ricci, K., Hallar, A. G., Clayton, M., Michalsky, J., Smirnov, A., Holben, B., and Barnard,
374 J. : How well do state-of-the-art techniques measuring the vertical profile of tropospheric aerosol extinction
375 compare? *J. Geophys. Res.*, 111, D05S07, doi:10.1029/2005JD005837, 2006.
- 376 She, C. Y., Alvarez II, R. J., Caldwell, L. M., and Krueger, D. A.: High-spectral-resolution Rayleigh-Mie lidar
377 measurement of aerosol and atmospheric profiles, *Opt. Lett.*, 17, 541-543, 1992.
- 378 Shinozuka, Y., Saide, P. E., Ferrada, G. A., Burton, S. P., Ferrare, R. A., Doherty, S. J., Gordon, H., Longo, K., Mallet,,
379 M., Feng, Y., Wang, Q., Cheng, Y., Dobracki, A., Freitag, S., Howell, S. G., LeBlanc, S., Flynn, C., Segal-
380 Rozenhaimer, M., Pistone, K., Podolske, J. R., Stith, E. J., Bennett, J. R., Carmichael, G. R., da Silva, A.,
381 Govindaraju, R., Leung, R., Zhang, Y., Pfister, L., Ryoo, J.-M., Redemann, J., Wood, R., and Zuidema, P.: Modeling
382 of the smoky troposphere of the southeast Atlantic: a comparison to ORACLES airborne observations from
383 September of 2016, *Atmos. Chem. Phys.*, 20, 11491-11526, doi:10.5194/acp-20-11491-2020, 2020.
- 384 Shipley, S. T., Tracy, D. H., Eloranta, E. W., Tauger, J. T., Stroga, J. T., Roesler, F. L., and Weinman, J. A.: High
385 spectral resolution lidar to measure optical scattering properties of atmospheric aerosols. 1. Theory and
386 instrumentation, *Appl. Optics*, 22, 3716-3724, 1983.
- 387 Stein, A.F., Draxler, R. R., Rolph, G. D., Stunder, B. J. B., Cohen, M. D., and Ngan, F.: NOAA's HYSPLIT
388 atmospheric transport and dispersion modeling system, *B. Am. Meteorol. Soc.*, 96, 2059-2077, doi:10.1175/BAMS-
389 D-14-00110.1, 2015.
- 390 Veselovskii, I., Kolgotin, A., Grazianov, V., Müller, D., Wandinger, U., and Whiteman, D. N.: Inversion with
391 regularization for the retrieval of tropospheric aerosol parameters from multi-wavelength lidar sounding, *Appl.*
392 *Optics*, 41, 3685-3699, 2002.
- 393 Wilcox, E. M.: Stratocumulus cloud thickening beneath layers of absorbing smoke aerosol, *Atmos. Chem. Phys.*, 10,
394 11769-11777, doi:10.5194/acp-10-11769-2010, 2010.
- 395 Wilcox, E. M.: Direct and semi-direct radiative forcing of smoke aerosols over clouds, *Atmos. Chem. Phys.*, 12, 139-
396 149, doi:10.5194/acp-12-139-2012, 2012.
- 397 Yamaguchi T, Feingold, G., Kazil, J., and McComiskey, A.: Stratocumulus to cumulus transition in the presence of
398 elevated smoke layers. *Geophys. Res. Lett.*, 42: 10478–10485, 2015.
- 399 Zhang Z., Meyer, K., Yu, H., Platnick, S., Colarco, P. R., Liu, Z., and Oreopoulos, L.: Shortwave direct radiative
400 effects of above-cloud aerosols over global oceans derived from 8 years of CALIPSO and MODIS observations,
401 *Atmos. Chem. Phys.*, 16, 2877-2900, doi:10.5194/acp-16-2877-2016, 2016.
- 402 Zhang, X., Mao, M., Yin, Y., and Tang, S.: The absorption Ångström exponent of black carbon with brown coatings:
403 effects of aerosol microphysics and parameterization, *Atmos. Chem. Phys.*, 20, 9701-9711, doi:10.5194/acp-20-
404 9701-2020, 2020.
- 405 Zuidema, P., Redemann, J., Haywood, J., Wood, R., Piketh, S., Hipondoka, M., and Formenti, P.: Smoke and clouds
406 above the southeast Atlantic, *B. Am. Meteorol. Soc.*, 97, 1131-1135, doi:10.1175/BAMS-D-15-00082.1, 2016.
- 407 Zuidema, P., Sedlacek III, A. J. Flynn, C., Springston, S., Delgado, R., Zhang, J., Aiken, A. C., Koontz, A., and
408 Muradyan, P.: The Ascension Island boundary layer in the remote Southeast Atlantic is often smoky, *Geophys. Res.*
409 *Lett.*, 45, 4456-4465, doi:10.1002/2017/GL076926, 2018.
- 410



411
412
413

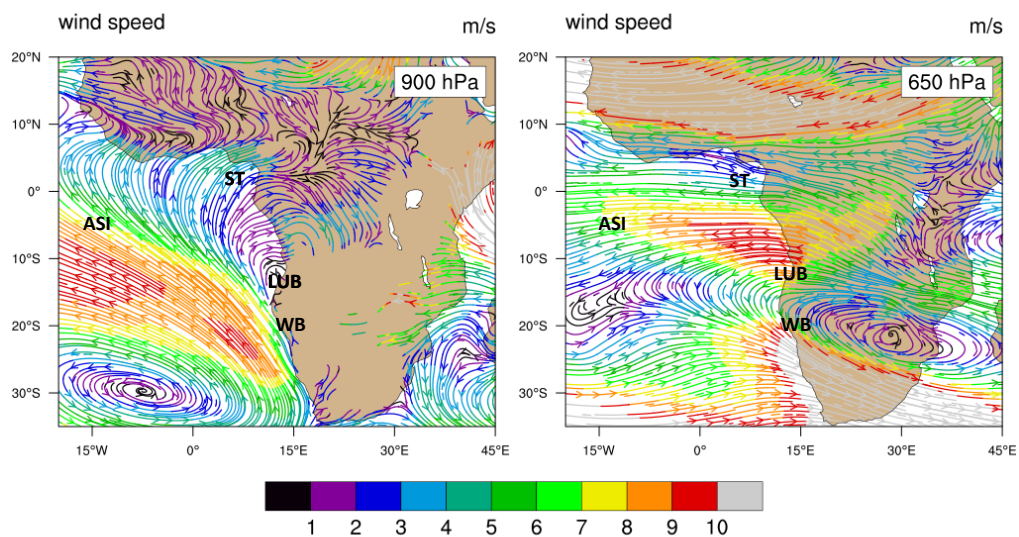
Table 1: Averaging area, flight time periods, the duration over water and number of HYSPLIT backward trajectories, and number of HSRL-2 profiles in each grid box used in the study.

Box	Averaging Area	Averaging Days	Time of Day	Duration in Hours Over Water at 3.5 km	Number of Profiles
A	11° S-9° S; 1° W-1° E	9/12,16	11:00 UTC	44.3±7.0 (N = 19)	50
B	10° S-8° S; 8° E-10° E	9/12,16,18	10:00 UTC	14.9±4.5 (N = 27)	56
C	16° S-14° S; 4° E-6° E	9/12,16	13:00 UTC	40.4±7.2 (N = 19)	51
D	14° S-12° S; 10° E-12° E	9/18,24	09:00 UTC	5.5±2.0 (N = 27)	46
E	23° S-21° S; 8° E-10° E	9/20,22	14:00 UTC	-	36

414



415

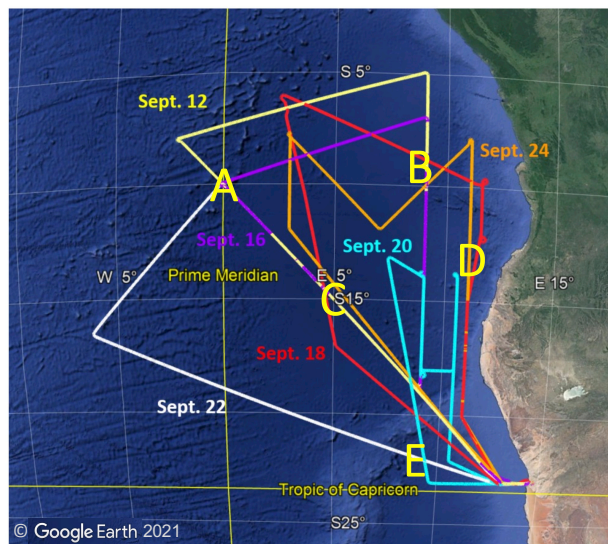


416
417
418
419
420
421

Figure 1: MERRA2 monthly mean reanalysis of 900 and 650 hPa streamlines for September 2021. Stations marked are Ascension Island (ASI), Lubango (LUB), a long-term AERONET site at 2 km elevation, and Walvis Bay (WB), where ER-2 flights originated from during the September 2021 ORACLES IOP. Flights in August 2017 and September/October 2018 originated from São Tomé (ST).



422

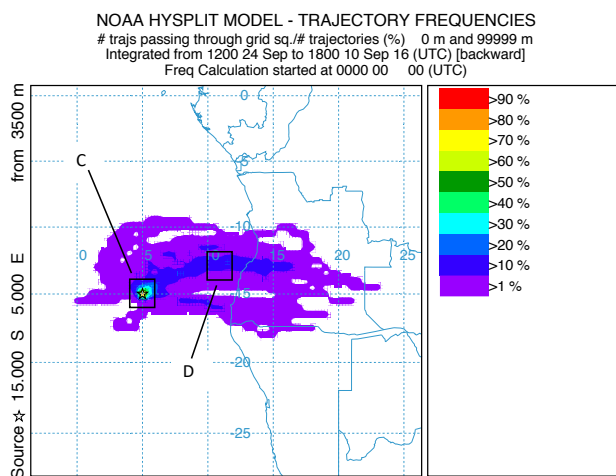
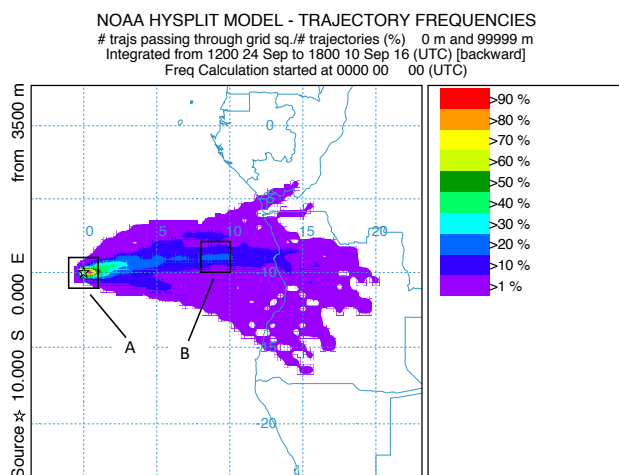


423
424
425
426

Figure 2: HSRL-2 science data flight tracks during the September 2016 IOP.



427

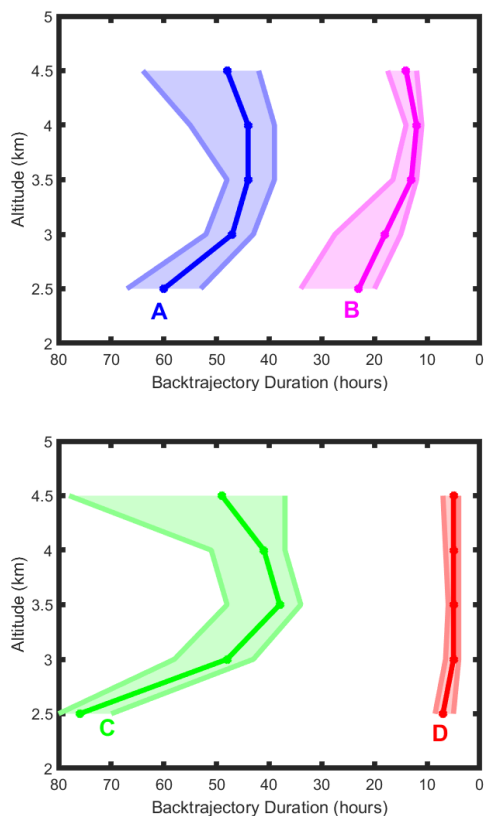


428
429
430
431
432
433

Figure 3: Frequency distribution of 48-hour backward trajectories of air parcels arriving at 3500 m above the centers of grid boxes A and C over the time period of the campaign. Grid boxes B and D are upstream of grid boxes A and C, respectively.



434

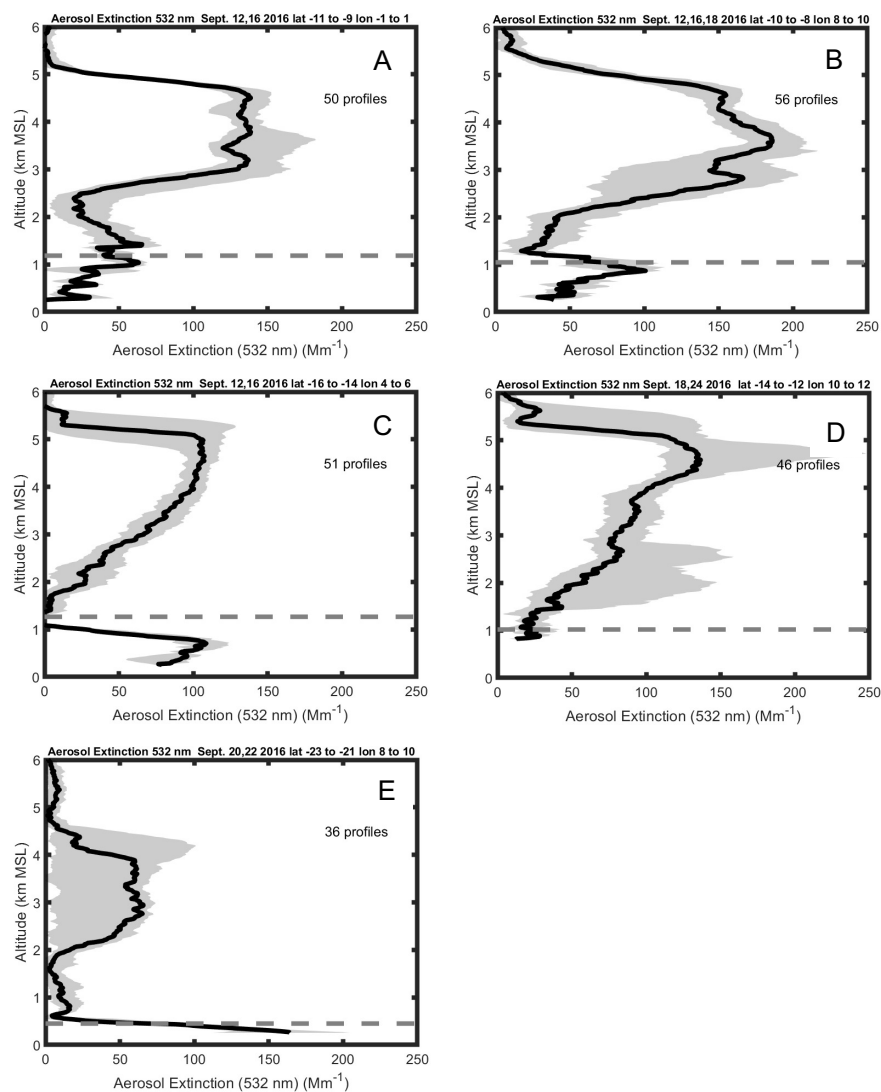


435
436
437
438
439
440
441
442

Figure 4: Duration of time spent over water of air parcels arriving at grid boxes marked on the figure. Solid lines are median values and the shaded portion are the range of the 75th and 25th percentile. The number of trajectories used for the calculation are in Table 1. Trajectory hours are shown in reverse to correspond to the map in Fig. 3.



443

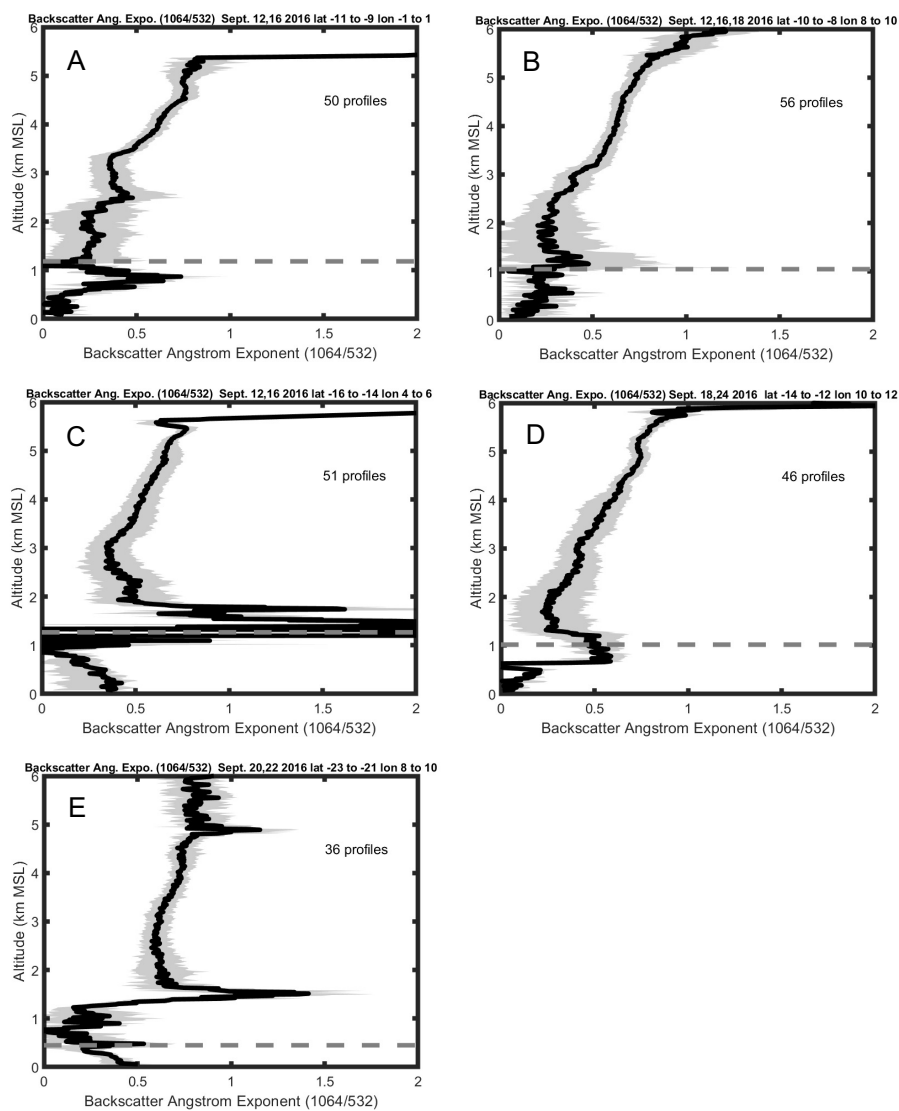


444
445
446
447
448
449

Figure 5: Average vertical profiles of the aerosol extinction coefficient at 532 nm in grid boxes A (upper left), B (upper right), C (middle left), D (middle right) and E (lower left). The averaging area, dates of flights and total number of one-minute profiles are also shown. The dark line represents the median value and grey shades contain the 25th to 75th percentiles. Dashed line refers to the mean cloud top height.



450

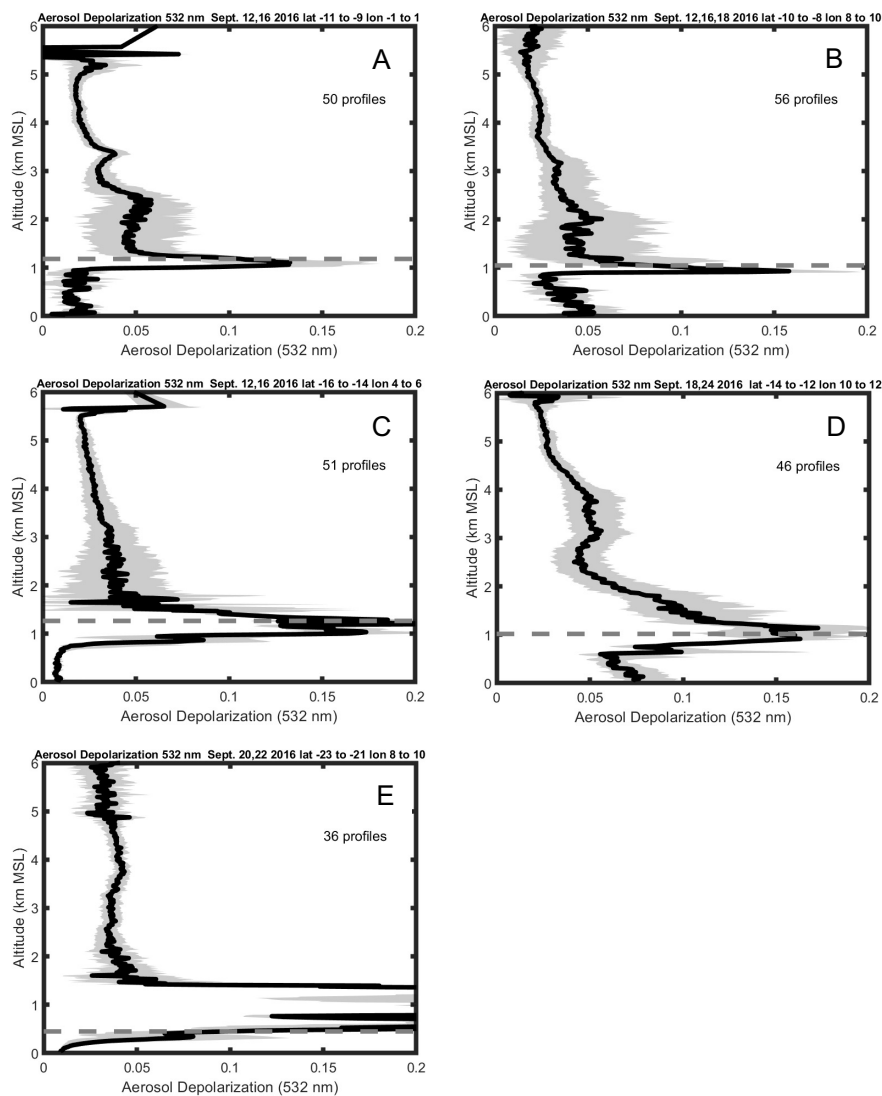


451
452
453
454

Figure 6: As in Fig. 5 but for the Wavelength Dependent Backscatter Ångström exponent between 1064 and 532 nm.



455

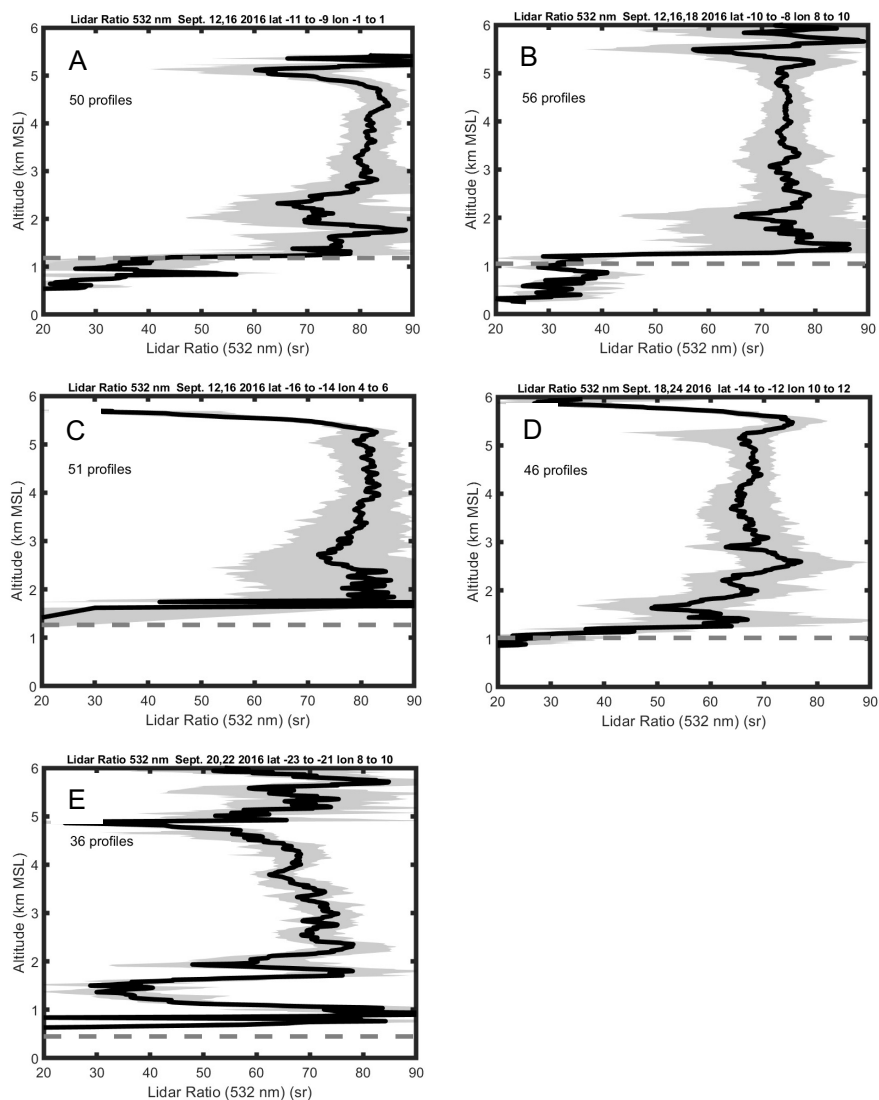


456
457
458
459

Figure 7: As in Fig. 5 but for the aerosol depolarization at 532 nm.



460

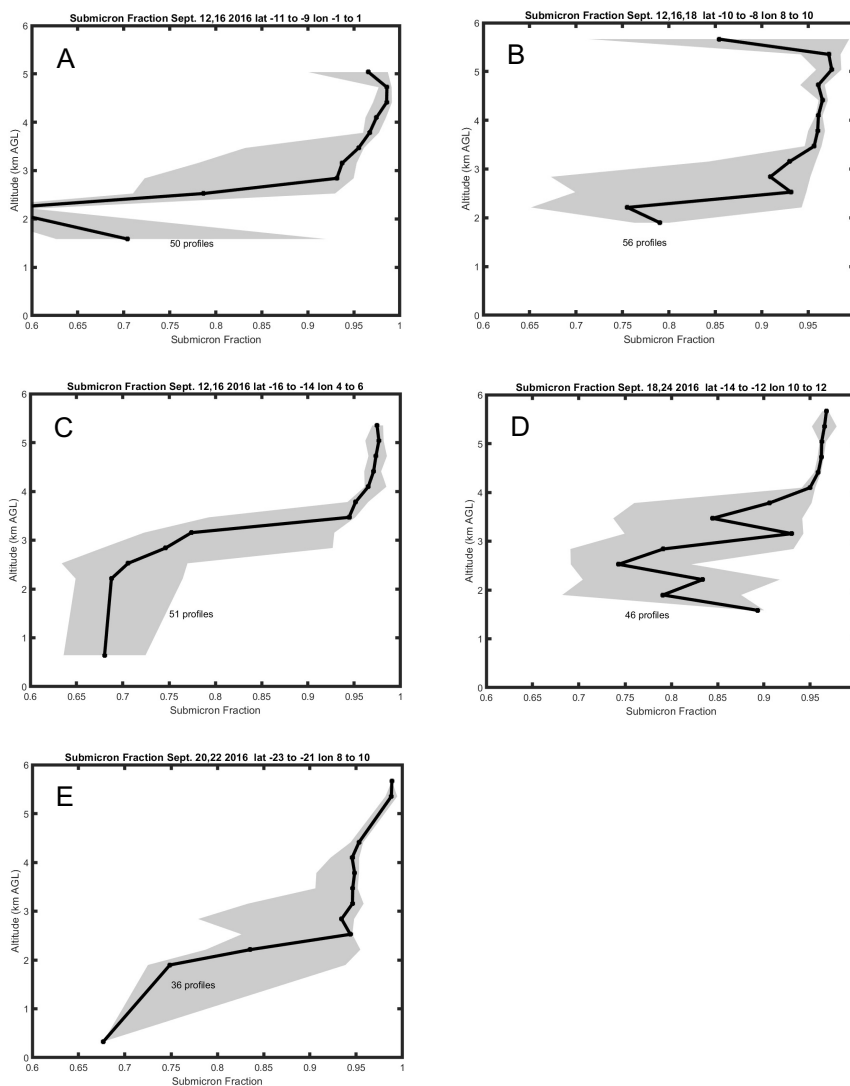


461
462
463

Figure 8: As in Fig. 5 but for the Lidar Ratio at 532 nm.



464

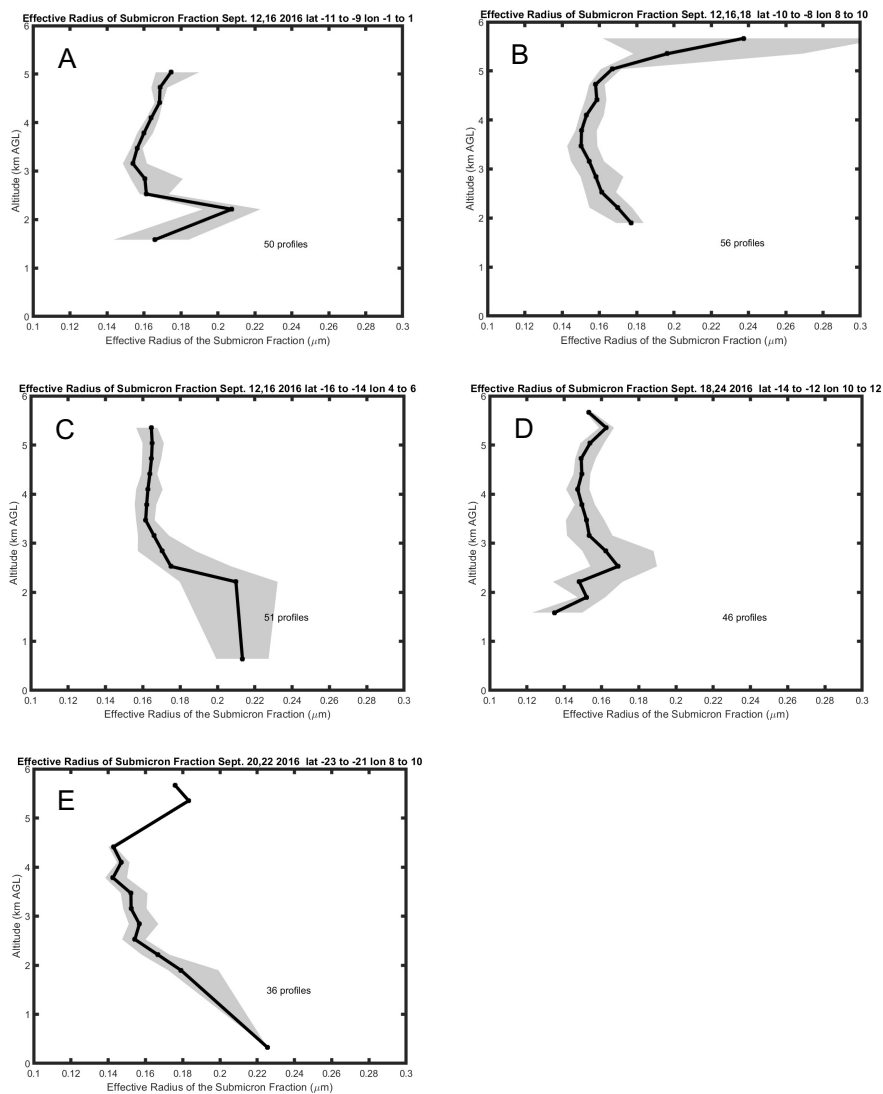


465
466
467
468
469
470

Figure 9: Average vertical profiles of the submicron fraction in grid boxes A (upper left), B (upper right), C (middle left), D (middle right) and E (lower left). The averaging area, dates of flights and total number of one-minute profiles in the average are also shown. The dark line represents the median value and grey shades contain the 25th to 75th percentiles.



471



472
473

Figure 10: As in Fig. 9 but for the effective radius of the submicron fraction.